A Carbazole-Based Hole Transport Polymer for Methylammonium-Free Tin-Lead Perovskite Solar Cells with Enhanced Efficiency and Stability

Jiantao Wang[1§], Zhenhua Yu[1§], Daniel D. Astridge[2], Zhenyi Ni[1], Liang Zhao[1], Bo Chen[1], Mengru Wang[1], Ying Zhou[1], Guang Yang[1], Xuezeng Dai[1], Alan Sellinger[2], and Jinsong Huang[1,3]*

[1]Department of Applied Physical Sciences, University of North Carolina at Chapel Hill, USA

[2]Department of Chemistry, Colorado School of Mines, USA

[3]Department of Chemistry, University of North Carolina at Chapel Hill, USA

Abstract: As the most commonly used hole transport material (HTM) in tin-lead (Sn-Pb) perovskite solar cells (PSCs), poly(3,4-ethylenedioxythiophene) polystyrenesulfonate (PEDOT:PSS) limits the power conversion efficiency (PCE) and stability of the PSCs due to its acidic characteristics. Herein, an easily synthesized polymer HTM poly[(phenyl)imino[9-(2-ethylhexyl)carbazole]-2,7-diyl] (CzAn) with a shallow highest occupied molecular orbital (HOMO) level of -4.95 eV is used in a p-i-n structure, methylammonium-free, Sn-Pb PSC to replace PEDOT:PSS. Upon optimization using doping and surface engineering, high quality Sn-Pb PSCs could be successfully fabricated, boosting the PCE to 22.6% compared with 21.2% for PEDOT:PSS. The perovskite films prepared on the modified CzAn HTM possess improved crystallinity, reduced trap-state density, and larger carrier mobility resulting in PSCs with greatly improved stability.

Keywords: hole-transport material, polymer, Sn-Pb perovskite solar cells, current density, stability

§ J.W. and Z.Y. contributed to this work equally.

*Correspondence should go to J. Huang E-mail: jhuang@unc.edu

1. Introduction

Metal halide perovskites have attracted extensive attention in the optoelectronics community due to their superior properties such as composition-dependent tunable bandgap (E_g), low-cost solution-processing, and rapidly increasing device performance.[1] Lead (Pb)-based halide single-junction perovskite solar cells (PSC) have achieved power conversion efficiencies (PCE) over 25%, which makes them a very competitive candidate in next-generation photovoltaic technologies.[2] To further improve the PCE close to the Shockley-Queisser efficiency limit, the bandgap of the perovskite absorbers requires narrowing, which is typically achieved by adding tin ions (Sn^{2+}) to replace a portion of the Pb^{2+} ions.[3] Sn-Pb alloyed perovskites have a lower bandgap of 1.21 eV when the Sn/Pb ratio is ≈1, which is the optimal composition to build perovskite-perovskite tandems.[4] The narrow bandgap Sn-Pb PSCs can be paired with the wide bandgap perovskite to form all-perovskite tandem solar cells, whose PCEs have already been demonstrated to surpass that of the top-performing single-junction PSCs.[5] However, one serious concern for Sn-Pb PSCs is their poorer stability than their pure lead-based counterparts.[6]

As the most commonly used HTM in Sn-Pb PSCs, poly(3,4-ethylenedioxythiophene)-poly(styrenesulfonate) (PEDOT:PSS) has advantages of good wetting for reproducible perovskite solution deposition, and appropriate energy levels for efficient hole extraction from Sn-Pb perovskites.[7] However, the PEDOT:PSS HTM accelerates perovskite degradation due to its corrosive acidic characteristics.[8] To replace PEDOT:PSS in Sn-Pb PSCs, three classes of HTMs have been investigated: inorganic HTMs, organic small-molecule HTMs, and polymer HTMs. Inorganic HTMs such as nickel oxide (NiO_x) were reported as a new candidate in Sn-Pb alloyed PSCs, but the device efficiencies were still lower than those using PEDOT:PSS.[9] Recently, Gaurav et al. employed an organic small-molecule based monolayer as HTM in Sn-Pb PSCs and obtained a higher PCE.[8a] However, the sensitive adsorption process of these self-assembled monolayers leads to defects and pinholes in the HTM, that in turn leads to reduced reproducibility of PSCs.[8a, 10] Polymer HTMs generally have facile processibility and better reproducibility, which holds better potential to replace PEDOT:PSS.[11] For instance, poly[bis(4-phenyl)(2,4,6-trimethylphenyl)amine] (PTAA), a widely used HTM in pure Pb PSCs, has achieved an enhanced PCE and thermal stability compared with PEDOT:PSS in Sn-Pb PSCs.[12] However, the mismatched energy levels between PTAA and Sn-Pb perovskites still limits the efficiency of Sn-Pb PSCs. Therefore, it is urgent to find a superior polymer HTM for Sn-Pb PSCs.

In this work, we report a polymer HTM poly[(phenyl)imino[9-(2-ethylhexyl)carbazole]-2,7-diyl] (CzAn) for use in high efficiency and highly stable methylammonium (MA)-free Sn-Pb PSCs. The CzAn HTM has energy levels well matched for the Sn-Pb layer and when modified with an ultrathin poly(methyl methacrylate) (PMMA) layer, leads to improved wettability to ensure good adhesion of the perovskite layer. A trace amount of 2,3,5,6-tetrafluoro-7,7,8,8-tetracyanoquinodimethane (F4TCNQ) is used as a dopant to enhance the hole conductivity while neutral PEDOT is added to help further tune the energy level of the CzAn HTM. Perovskite films deposited on the modified CzAn show reduced trap-state density and improved carrier transport, that enhances the PSC internal quantum efficiency and current density. Finally, the CzAn based Sn-Pb PSCs achieved a remarkable PCE of 22.6% with enhanced stability.

2. Results and Discussion

The device structure and the molecular structure of CzAn are shown in **Figure 1a**. The methylamine (MA)-free Sn-Pb perovskite has a composition of $FA_{0.8}Cs_{0.2}Sn_{0.5}Pb_{0.5}I_3$ and has shown better stability than volatile-MA embedded perovskites under heat and light.[8b, 13] To further improve the device PCE, a passivation layer was processed on top of the Sn-Pb layer by depositing benzylhydrazine hydrochloride (BHC) and phenyl-C_{61}-butyric acid methyl ester ($PC_{61}BM$) consecutively.[14] The fabrication details can be found in the experimental section. CzAn has a highest occupied molecular orbital (HOMO) level of -4.95 eV and a lowest unoccupied molecular orbital (LUMO) level of -2.01 eV[11], which is suitable for Sn-Pb PSCs, as shown in **Figure S1**. The CzAn has a facile synthesis, which can be found in the experimental section, and good thermal stability with a glass transition temperature (T_g) of 146 °C and decomposition temperature (T_d) of 362 °C, making it a promising HTM for Sn-Pb PSCs.[15] This polymer has been applied in p-i-n structured perovskite solar cells to yield an efficiency of 17.2% using $(FA_{0.79}MA_{0.16}Cs_{0.05})Pb(I_{0.84}Br_{0.16})_3$.[11] When we employed CzAn alone in p-i-n structured Sn-Pb PSCs, we found that it was too hydrophobic, leading to discontinuous perovskite thin films, as shown in **Figure 1b**. To enhance surface hydrophilicity of CzAn, we coated an ultra-thin PMMA layer on top, as the carbonyl groups in PMMA enhance wetting with both perovskites and the HTM[16], as shown by the continuous perovskite film coverage in **Figure 1b**. However, the CzAn/PMMA HTM did not lead to higher efficiency Sn-Pb PSCs, as shown by the photocurrent curves in **Figure 1c**. We hypothesized that this was caused by the relatively low hole conductivity of CzAn. To test this, we added to the CzAn layer the commonly used p-type dopants 2,3,5,6-tetrafluoro-7,7,8,8-tetracyanoquinodimethane

(F4TCNQ), tris(pentafluorophenyl)borane (BCF) and [9-(2-ethylhexyl)-N2,N2,N7,N7-tetrakis(4-methoxyphenyl)-9H-carbazole-2,7-diamine bis-(trifluoromethanesulfonyl)imide] (EH44-ox).[15, 17] All dopant concentrations were 1 wt % (weight ratio) relative to CzAn. As shown in **Figure 1c**, F4TCNQ doped CzAn resulted in the best device efficiency. We then optimized the thickness of the doped CzAn HTM by tuning the concentration of the precursor solution. As shown in **Figure S2**, 1 mg mL^{-1} doped CzAn resulted in the best device efficiency. Though the doped polymer HTM led to high short-circuit current density (J_{sc}) and fill factor (FF), the open-circuit voltage (V_{oc}) was still lower than 0.80 V, which may be due to the slightly mismatched energy level between the Sn-Pb perovskite and HTM. To address this, we added a small amount of neutral PEDOT (HTL Solar 3, Ossila), that is a commercial dispersion in toluene without the PSS ionomer, to adjust the work function of the doped CzAn HTM. As shown in **Figure 1d**, 2% v/v (v/v: volume ratio) neutral PEDOT notably enhanced the V_{oc} to 0.85 V, which is comparable with the device based on PEDOT:PSS HTM.

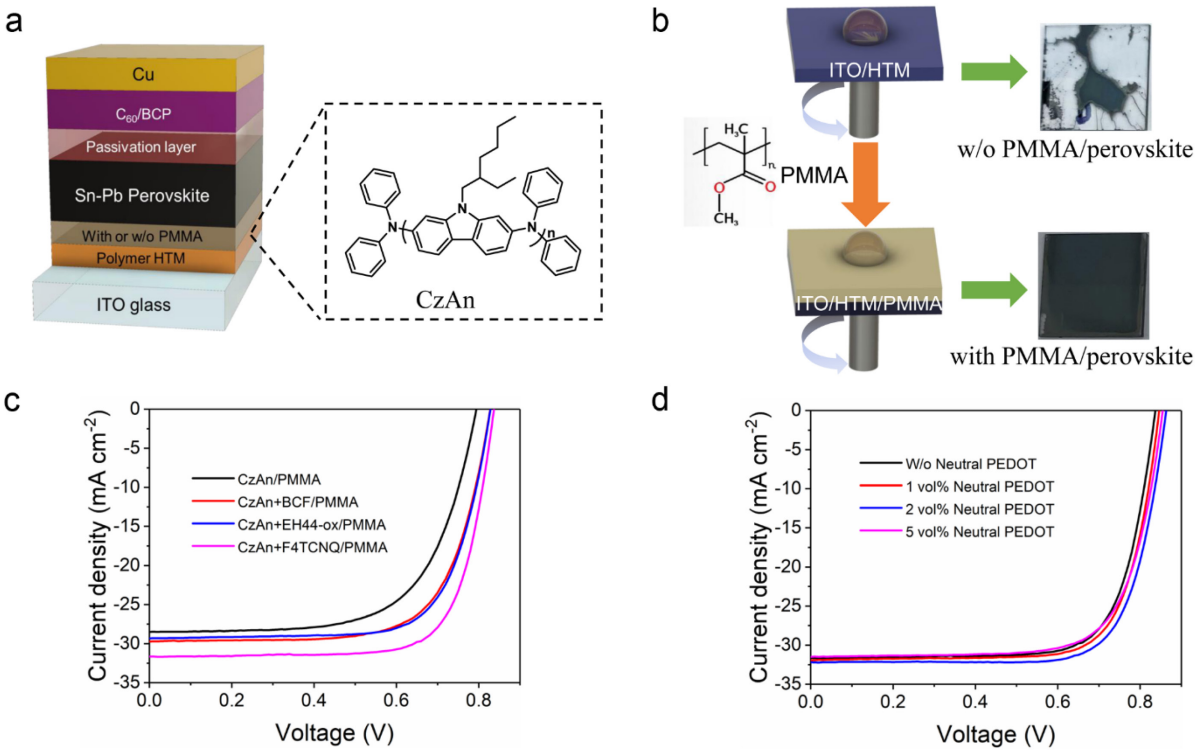

Figure 1. Modification process of the CzAn polymer HTM. (a) Device structure of Sn-Pb PSCs and molecular structure of CzAn. (b) Images of perovskite coverage on HTM with and without PMMA. (c) Reverse scan current density-voltage (*J-V*) curves of Sn-Pb PSCs based on CzAn HTM with varying p-type dopants and, (d) different amounts of neutral PEDOT in the CzAn layer.

To investigate the impact of PMMA on CzAn, we conducted atomic force microscopy (AFM) under height mode to study the surface morphologies of CzAn with and without PMMA (**Figure S3**). The coating of CzAn by PMMA resulted in a smoother surface, revealed by the decreased root-mean-square (RMS) roughness from 5.188 nm to 4.168 nm. We tuned the PMMA coverage by changing its solution concentration, and found it impacted the device performance dramatically. As shown in **Figure S4**, the optimal concentration of PMMA for the highest device PCE was 0.2 mg mL^{-1}. This can be well explained by the insulating nature of PMMA, in addition to the reported passivation of PMMA to PSCs.[18] Using this optimized PMMA thickness (estimated to be 4 - 8 nm)[19], we fabricated Sn-Pb PSCs with the configuration of ITO/polymer HTM/PMMA/Sn-Pb perovskite/passivation layer/C_{60}/BCP/Cu (**Figure 1a**), in which the polymer HTM refers to the modified CzAn and PEDOT:PSS counterparts.

We measured the device performance by collecting the current density-voltage (*J-V*) curves with forward and reverse scans of the fabricated devices. The champion devices based on PEDOT:PSS and CzAn are plotted in **Figure 2a**, and their detailed parameters are listed in **Table 1**. The CzAn based devices obtain the highest PCE of 22.6%, with a V_{oc} of 0.87 V, a J_{sc} of 32.6 mA cm^{-2} and an FF of 79.6%, while the optimized devices with PEDOT:PSS HTM had a PCE of 21.2%, a V_{oc} of 0.85 V, a J_{sc} of 31.3 mA cm^{-2} and an FF of 79.8%. We also used insulating PMMA in PEDOT:PSS based devices, but inserting PMMA between PEDOT:PSS and perovskite reduced FF and J_{sc} compared with the pristine device, as shown in **Figure S4**. To understand how reproducible the HTMs are, we fabricated 20 devices for each type of device. The statistical distribution of their PCE, V_{oc}, J_{sc}, and FF are shown in **Figure 2b**. The calculated mean and standard deviation of V_{oc}, J_{sc}, FF and PCE for CzAn embodied devices are 0.85 ± 0.01 V, 31.89 ± 0.34 mA cm^{-2}, 77.86 ± 0.01 % and 21.12 ± 0.62 %, respectively. Those parameters for PEDOT:PSS based devices are 0.84 ± 0.01 V, 30.48 ± 0.52 mA cm^{-2}, 80.48 ± 0.01 % and 20.62 ± 0.50 %, respectively. From these, we conclude that the PCE increase of the devices with the modified CzAn HTM comes from the enhancement of V_{oc} and J_{sc}, despite a small decrease in FF likely caused by insulating PMMA.[16b]

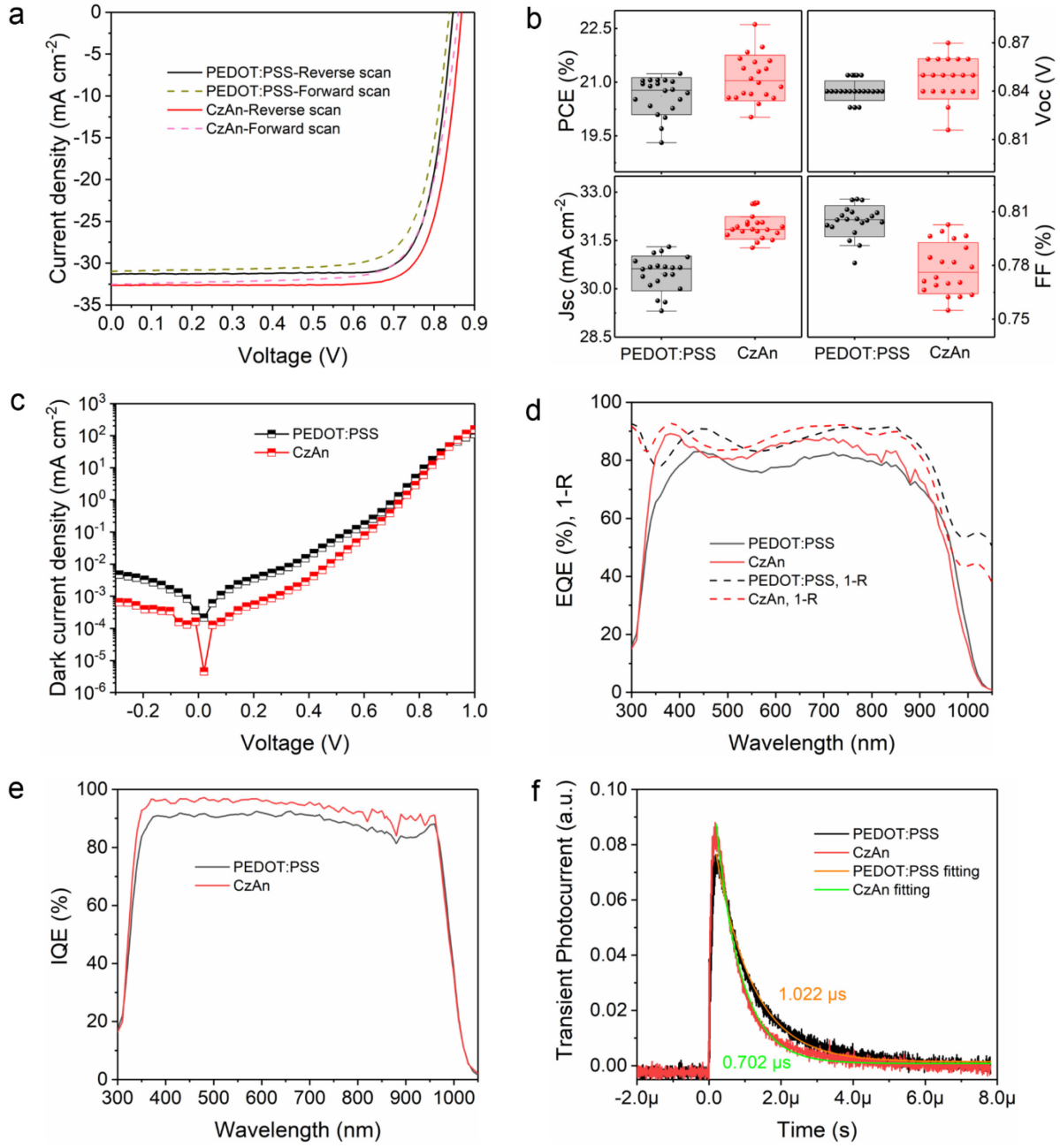

Figure 2. Device performance and characterization of Sn-Pb PSCs. (a) *J-V* curves with forward scan and reverse scan of champion devices based on PEDOT:PSS and CzAn. (b) Statistics of PCE, V_{oc}, J_{sc}, and FF of PSCs based on 20 devices. (c) Dark *J-V* curves. (d) External quantum efficiency (EQE) and reflected absorption. (e) Internal quantum efficiency (IQE). (f) Transient photocurrent (TPC) of PSCs based on PEDOT:PSS and CzAn HTMs.

Table 1. Photovoltaic performance parameters of the champion devices with PEDOT:PSS and CzAn as HTM.

Devices[a)]	Scan direction	V_{oc} [V]	J_{sc} [mA cm^{-2}]	FF [%]	PCE [%]

PEDOT:PSS	Forward scan	0.82	30.99	78.07	19.84
	Reverse scan	0.85	31.31	79.81	21.24
CzAn	Forward scan	0.82	32.54	79.26	21.15
	Reverse scan	0.87	32.64	79.62	22.61

[a)] Measured with 1 sun intensity illumination under AM 1.5 G.

We conducted device characterization to understand why CzAn enhances the device performance. To analyze the V_{oc} of the devices, we collected the *J-V* curves under dark conditions. As shown in **Figure 2c**, the leakage current density of the PEDOT:PSS based device is 10 times larger than the CzAn based device, The smaller dark current density of CzAn based device agrees with the increase of V_{oc}.[20] The reduced trap density of states (tDOS) in the CzAn based device was further demonstrated by the thermal admittance spectroscopy (TAS) results displayed in **Figure S5**. TAS is an established method that can quantitatively compare the trap density of states in the profiling energy depth.[21] Two shallow trap bands (0.3 - 0.35 eV and 0.35 - 0.48 eV) and one deeper trap band (> 0.48 eV) were found in the Sn-Pb PSCs. The tDOS of PEDOT:PSS based PSCs in the entire trap depth is higher, which indicates the existence of abundant surface and bulk defects that result in lower V_{oc}.

To analyze the increase of the J_{sc}, we measured the external quantum efficiency (EQE) curves of two typical devices with CzAn and PEDOT:PSS HTMs. As shown in **Figure 2d**, the EQE of the CzAn based device is higher than that using PEDOT:PSS in the wavelength range of 350 - 950 nm. The J_{sc} integrated from the EQE curve for the CzAn based device is 30.3 mA cm^{-2}, 5% higher than that based on PEDOT:PSS (28.9 mA cm^{-2}), which agrees with *J-V* curves. We observed that the EQE peaks shifted for the two types of devices, which could be caused by the different optical interference. To examine what is the actual charge collection efficiency, the internal quantum efficiency needs to be derived. To that end, we compared their optical losses by measuring the device reflectance. The absorption in the devices at each wavelength can be derived from 100%-reflectance (R) by assuming other parasitic absorption is negligible. The dashed lines in **Figure 2d** show the absorption curves calculated from the reflection spectra of the two types of devices measured using a spectrometer with an integration sphere. The actual absorption curves have the same trend with the corresponding EQE curves, that confirms that the shape change of EQE curves is primarily derived from the interference. We further obtained the internal quantum efficiency (IQE) spectra using EQE and (1-R):

$$IQE = EQE/(1 - R) \quad (1)$$

As shown in **Figure 2e**, the IQE of CzAn based device displayed an overall 5% enhancement in the whole absorption spectrum range of 350 nm - 950 nm. We analyzed the carrier transport across the device by performing the transient photocurrent (TPC) measurements.[22] The photocurrent produced a transient voltage signal on a 50 Ω resistor, that was recorded by an oscilloscope. As shown in **Figure 2f**, the transient time (τ) in CzAn based PSCs is 0.702 μs, shorter than that in PEDOT:PSS devices (1.022 μs). Even though the film thicknesses (L) of the perovskite layers are different, as shown in **Figure S8**, the larger diffusivity of the CzAn based device (D, $D=L^2/\tau$) mainly comes from a smaller τ. It reveals that the Sn-Pb perovskites grown on modified CzAn have an enhanced carrier transport capacity, that increases J_{sc}.[23] We have studied the trap density in perovskites and found that Sn-Pb perovskites grown on modified CzAn had smaller trap-state density, as shown in **Figure S5**, that explains the better mobility.

To study the origin of the better-quality Sn-Pb perovskites grown on modified CzAn, we studied the morphology and crystallinity using scanning electron microscopy (SEM) and XRD. As shown in **Figure S6**, Sn-Pb perovskite films are dense and pin-hole free. Some chemical residuals remained at the grain boundaries of the Sn-Pb perovskite on the modified CzAn, which might be assigned as SnF_2 additives that was added to precipitate oxidized Sn^{2+}.[24] Their cross-sectional SEM images are shown in **Figure 3a, b**. Perovskite films deposited on CzAn are relatively flat with smoother top and bottom surfaces, that is beneficial to form more intimate contacts with both sides. In contrast, perovskite film on PEDOT:PSS has obvious grain delamination with higher undulation on the top surface and fine grains at the bottom contact, which could allow for more recombination centers. As shown in **Figure 3c**, the intensity of XRD patterns of perovskite on CzAn/PMMA is higher than that on PEDOT:PSS. The full width at half maximum (FWHM) values at the typical perovskite characteristic peak of 13.92° are 0.1002° and 0.1258° for CzAn and PEDOT:PSS based samples, respectively. A higher XRD peak intensity for CzAn based perovskite film with smaller FWHM indicates a better film crystallinity, that explains the lower trap density in these perovskites.

To gain more insight on the optoelectronic properties of the perovskite deposited on the modified CzAn and PEDOT:PSS, we measured their UV-Vis-NIR absorption and photoluminescence (PL). As shown in **Figure S7**, both films have no obvious change of optical bandgap of 1.22 eV, but surprisingly the absorption of the Sn-Pb perovskite film on PEDOT:PSS is slightly stronger than that on modified CzAn. The measured Sn-Pb perovskite film thicknesses are 916.09 nm and 966.41 nm for the films deposited on modified CzAn and PEDOT:PSS, respectively (**Figure S8**), explaining the reduced absorption. This also explains

the observed difference of interference in the devices and thus changed EQE shapes. On the other hand, it suggests decreased recombination and enhanced charge collection in the thinner perovskite film on the modified CzAn as it had a higher J_{sc} despite weaker light absorption. We performed PL experiments of perovskite films on the half device stack of ITO/modified CzAn/perovskite and ITO/PEDOT:PSS/perovskite. As shown in **Figure 3d**, the CzAn based perovskite film has lower PL intensity no matter if the incident light came from the air side or glass side. As we have confirmed the deep charge trap density in the CzAn based perovskite film is lower, which corresponds to less trap-assisted recombination, the reduced PL emission can be explained by enhanced hole extraction to the HTM and then ITO.

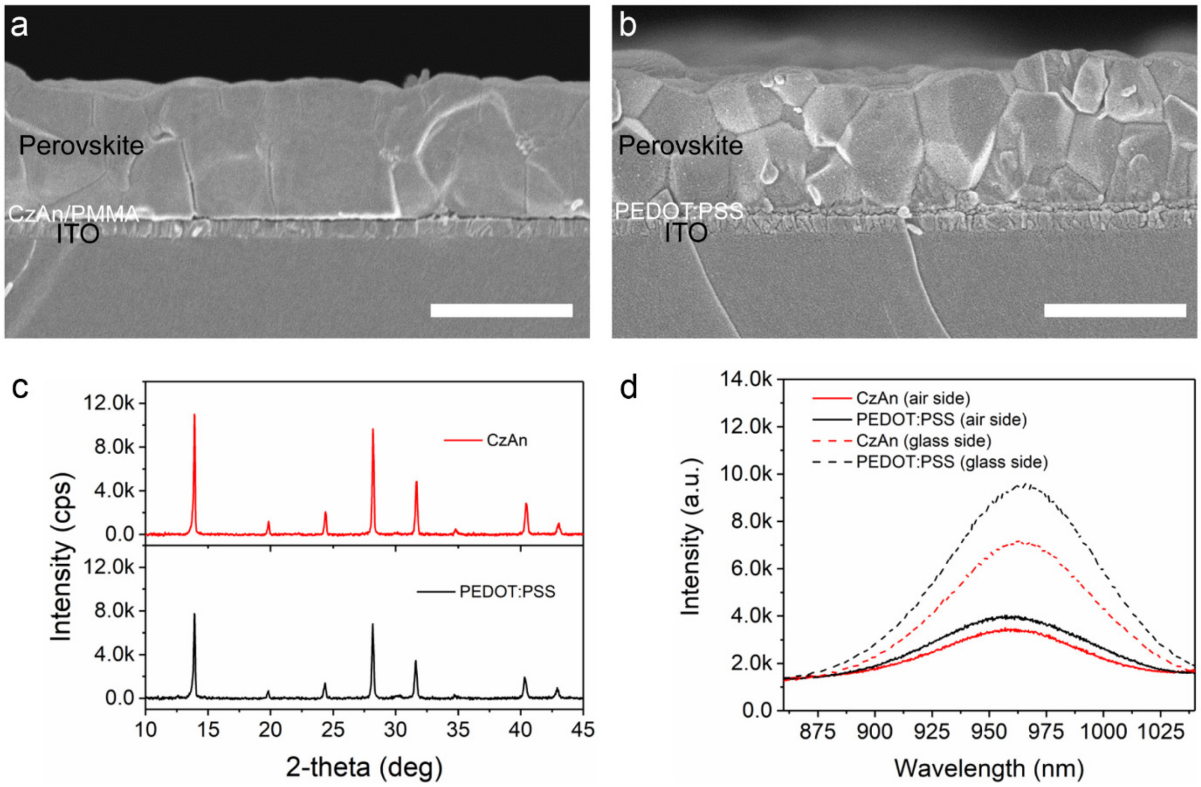

Figure 3. Characterizations of perovskite films. Cross-section morphology of perovskite deposited on (a) ITO/CzAn and (b) ITO/PEDOT:PSS, scale bar is 1 μm. (c) XRD patterns of perovskite films. (d) PL of perovskite films deposited on ITO/CzAn and ITO/PEDOT:PSS. Perovskite surfaces were covered a layer of perfluoro(1-butenyl vinyl ether) polymer (CYTOP) before the PL measurements.

To examine how the changed film quality affects the light stability of Sn-Pb perovskites, we studied the light generation of iodine (I_2) in these films, as it was reported to be the main reason for the rapid degradation of fully encapsulated Sn-Pb perovskites.[25] Perovskite films

deposited on modified CzAn or PEDOT:PSS were immersed into toluene to extract I_2 generated in films, as shown in **Figure S9**. By measuring the absorption spectra of the two toluene solutions after light soaking for different durations, the I_2 generation rate can be directly compared.[26] According to the absorption spectra as shown in **Figure 4a**, the I_2 generation rate in the Sn-Pb perovskite on modified CzAn is slower than that on PEDOT:PSS, that indicates the improved crystallinity helps stabilize Sn-Pb perovskites under illumination. We removed the films after light soaking for 5 h and 15 h and performed XRD on the films. The XRD peak intensities decreased over time (**Figure 4b**). The FWHM of the XRD peak at 13.92° increased to 0.1759° and 0.1277° relative to the initial measurements in **Figure 3c** for films on PEDOT:PSS and CzAn, respectively, after 15 h light soaking. The rate of degradation of the perovskite film on PEDOT:PSS is faster in terms of the more rapid increase of FWHM, that agree with the I_2 extracted into toluene data.

To study the stability of photovoltaic devices, we measured the stabilized power output (SPO) at the maximum power point (MPP). The devices used in this test had an initial efficiency of 20.1% and 21.3% for PEDOT:PSS and CzAn based devices, respectively. After testing for 600 s, the device with CzAn showed no PCE loss while the PCE of the PEDOT:PSS based device decreased to 16.9% (**Figure 4c**). Moreover, the shelf-life stability of encapsulated devices under ambient conditions was studied by measuring the device *J-V* curves. The CzAn based device retained 96% of the initial PCE after 1000 h storage while that for the PEDOT:PSS based device decreased to 91% (**Figure S10**). We plotted their *J-V* curves at 0 and 1000 h in **Figure 4d**. Even after 1000 h, the resultant PCE of 21.65% for CzAn based device is still higher than the initial PCE of 21.02% for PEDOT:PSS based device, as listed in **Table S1**.

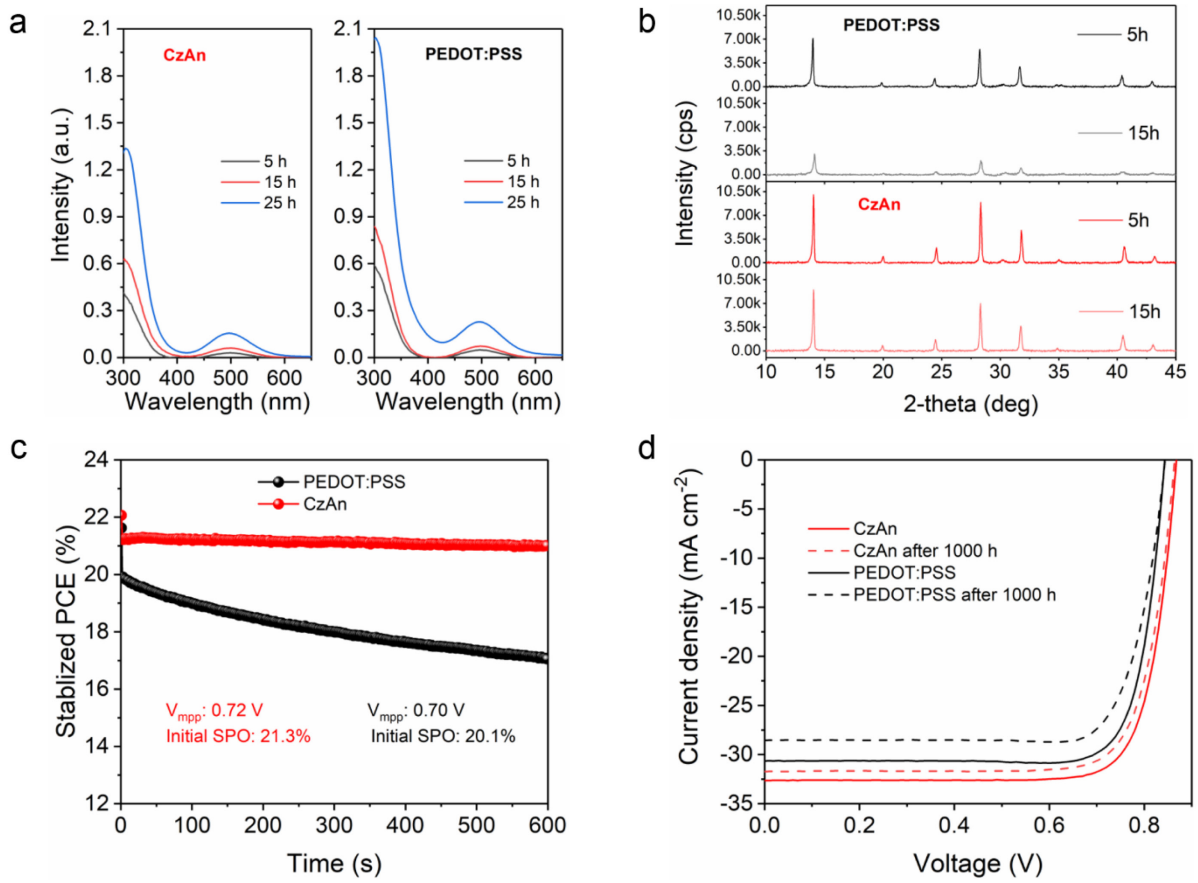

Figure 4. Stability measurements of perovskite films and devices. (a) Absorption spectra of the toluene in which perovskite films deposited on CzAn/PMMA or PEDOT:PSS were immersed under 1 sun illumination for 5 h, 15 h and 25 h. (b) XRD patterns of perovskite films deposited on CzAn/PMMA or PEDOT:PSS and immersed in toluene under 1 sun illumination for 5 h and 15 h. (c) Stabilized PCE output (SPO) of the typical devices based on PEDOT:PSS and CzAn. (d) *J-V* curves of Sn-Pb alloyed PSCs based on CzAn and PEDOT:PSS before and after storing for 1000 h.

3. Conclusion

In conclusion, we reported a modified CzAn polymer as HTM in Sn-Pb PSCs to obtain a remarkable PCE of 22.6% with enhanced stability. After modifying CzAn by doping and surface engineering, high quality Sn-Pb perovskites could be fabricated. Perovskite films deposited on the modified HTM showed improved crystallization, reduced trap-state density and better charge collection efficiency. Better film quality of perovskite deposited on the modified HTM compared with PEDOT:PSS contributed to an overall 5% increase of the internal quantum efficiency and the enhanced photocurrent density to 32.6 mA cm^{-2}. Finally, Sn-Pb PSCs using CzAn HTM shows improved stability over PEDOT:PSS from reduced I_2 generation under light exposure, stabilized PCE output (SPO) at MPP, and after 1000 h

encapsulated device storage. This work paves a way for utilizing custom prepared hole transport polymer to fabricate Sn-Pb PSCs with high-performance and it holds promise to further enhance the PCE and stability of integrated all-perovskite tandem solar cells.

Acknowledgement: This work was supported by the Solar Energy Technologies office within the U.S. Department of Energy, Office of Energy Efficiency and Renewable Energy, under Award Number DE-EE0008749.

4. Experimental Section

Materials: Unless otherwise stated, all the chemicals were purchased from Sigma-Aldrich and used as received. Formamidinium iodide (FAI) was purchased from GreatCell Solar. Lead(II) iodide (PbI_2) was purchased from TCI. C_{60} and $PC_{61}BM$ were purchased from Nano C. Benzylhydrazine hydrochloride (BHC) was purchased from Ambeed. PEDOT dispersion was purchased from Ossila. PEDOT:PSS dispersion was purchased from Heraeus. 2,7-dibromocarbazole was obtained from Francis Bélanger at Seqens-PCAS. Bis(tri-*tert*-butylphosphine) palladium (0) was purchased from Strem Chemicals. Aniline was purchased from Acros organics and vacuum distilled over KOH.

Synthesis: The synthesis of the carbazole monomer has been previously reported.[27] The polymer CzAn was scaled up from a previous synthesis.[11] Briefly, 2,7-dibromo-9-(2-ethylhexyl)-9H-carbazole (6.00 g, 13.7 mmol) and sodium *tert*-butoxide (3.60 g, 41.2 mmol) were added to an oven dried 250 mL Schlenk flask with a stir bar. The flask was then purged with vacuum and refilled with nitrogen three times. Aniline (1.14 mL, 13.7 mmol) was added via autopipette with positive nitrogen flow, followed by the palladium catalyst (0.250 g, 0.0489 mmol). Anhydrous toluene (100 mL) was added via syringe with stirring, and the mixture brought to 80°C. After 24 hours bromobenzene was added by autopipette with positive nitrogen flow. After 1 hour, diphenylamine was added with positive nitrogen flow. After an hour, the heat was turned off and the reaction allowed to cool to room temperature, whereupon tetrahydrofuran was added (50 mL) and allowed to stir for 15 minutes. The mixture was poured into cold stirring methanol which afforded yellow strands of polymer which were collected via vacuum filtration. The crude polymer was then dissolved in tetrahydrofuran and refluxed overnight with diethylammonium diethyldithiocarbamate to remove any residual palladium. The resulting golden solution was then precipitated in cold stirring methanol, and the polymer was collected by vacuum filtration and dried. The polymer was again dissolved in tetrahydrofuran and precipitated into an ethyl acetate – acetone 50:50% v/v solution to remove

low molecular weight chains, followed by vacuum filtration and overnight drying in a vacuum oven at 50°C to afford a bright yellow solid, 3.68 g, 80 %.

Device Fabrication: 1.5×1.5 cm^2 patterned ITO substrates were cleaned with acetone and isopropyl alcohol respectively under ultrasonication for 15 min. Substrates dried by nitrogen were further cleaned by UV ozone for 15 min before the spin-coating process in a nitrogen filled glovebox. CzAn, 1 mg mL^{-1} dissolved in chlorobenzene (CB), was prepared with the addition of 1 wt % F4-TCNQ and 2% v/v PEDOT dispersion. The CzAn HTM solutions were used without filtering and were spin-coated onto ITO substrates at 5000 rpm for 30 s and annealed at 130 ℃ for 10 min. 0.1 - 0.3 mg mL^{-1} PMMA dissolved in acetonitrile (ACN) was spin-coated on the resulting substrates at 5000 rpm for 30 s and annealed at 130 ℃ for 10 min. The PEDOT:PSS was processed by spin-coating at 4000 rpm for 30 s and annealed at 150 ℃ for 10 min in ambient air. 2 M perovskite $Cs_{0.2}FA_{0.8}Pb_{0.5}Sn_{0.5}I_3$ solution was prepared by dissolving 0.4 M CsI, 1.6 M FAI, 1 M PbI_2 and 1 M SnI_2 together with additives 0.1 M SnF_2 and 0.02 M PEACl in 1 mL DMF/DMSO (v/v 3:1) and stirred overnight. Perovskite solutions were filtered using 0.22 μm filters. Additives including 3% v/v DMSO, 1.6 mg mL^{-1} BHC, 0.02 M $RbPbI_3$, 0.05 M $Cs_{0.2}FA_{0.8}I$, 0.01 M BaI_2 were added into the precursor solution before processing. Perovskite films were deposited by spin-coating at 1500 rpm for 10 s and 3500 rpm for 45 s. 140 μL ethyl acetate (EA) was dispensed on the wet film 10 s before the spinning ended. The resultant films were annealed at 130 ℃ for 7 min then 85 ℃ for 30 min. BHC (0.1 mg mL^{-1} dissolved in EA) and $PC_{61}BM$ (10 mg mL^{-1} dissolved in CB) were spin-coated on perovskite films and annealed at 70 ℃ for 5 min successively. All the substrates were transferred to the thermal evaporator for the deposition of C_{60} (22.5 nm), BCP (5 nm) and Cu (90 nm). All the devices were encapsulated in the glovebox before measurements and characterizations.

Measurements and Characterizations: The current density-voltage (*J-V*) curves were measured using a source meter (Keithley 2400) and a solar simulator (Newport xenon lamp). The light intensity was calibrated to 100 mW cm^{-2} by a reference silicon solar cell (Newport 91150V) with KG-5 filter. The stabilized power outputs (SPO) were measured by detecting the current density under the maximum-power-point voltage. A photomask with 0.059 cm^2 area was used to eliminate the edge effect for efficiency measurements. The external quantum efficiency (EQE) curves were recorded by a Newport QE measurement kit with a monochromatic light, in which the light intensity at every wavelength from 300 to 1100 nm was calibrated with a silicon detector before measurements. The measurements of trap density of states (*t*DOS) were performed using an Agilent E4980A precision LCR meter. The transient photocurrent (TPC)

measurements were conducted using an oscilloscope (DOS-X 3104A), and an attenuated 337 nm pulsed laser (SRS NL 100 Nitrogen Laser, frequency of 10 Hz and pulse width of <3.5 ns) was used. The reflectance and absorption spectra were collected by a Thermo Scientific Evolution 201 UV-vis-NIR spectrophotometer. The surface topographies were detected by atomic force microscopy (AFM, Asylum Research MFP3D). The ultraviolet photoelectron spectroscopy (UPS, Kratos Axis Supra) was performed with a non-monochromated He Iα photon source (hν=21.2 eV) to measue the HOMO of HTMs. The surface and cross-section morphologies of perovskite films were recorded by scanning electron microscopy (SEM, Hitachi S-4700). The XRD patterns were obtained using an X-ray diffractometer (Rigaku SmartLab) and the height of films was calibrated before each measurement. The photoluminescence (PL) curves were measured using a Horiba iHR320 Imaging Spectrometer at room temperature under a 532 nm excitation light.

Supporting Information

Supporting Information is available from the Wiley Online Library or from the author.

Received: ((will be filled in by the editorial staff))
Revised: ((will be filled in by the editorial staff))
Published online: ((will be filled in by the editorial staff))

References

[1] a) A. Kojima, K. Teshima, Y. Shirai, T. Miyasaka, *Journal of The American Chemical Society* **2009**, 131, 6050; b) M. M. Lee, J. Teuscher, T. Miyasaka, T. N. Murakami, H. J. Snaith, *Science* **2012**, 338, 643; c) H. S. Kim, C. R. Lee, J. H. Im, K. B. Lee, T. Moehl, A. Marchioro, S. J. Moon, R. Humphry-Baker, J. H. Yum, J. E. Moser, M. Gratzel, N. G. Park, *Sci Rep* **2012**, 2, 591; d) N. J. Jeon, J. H. Noh, Y. C. Kim, W. S. Yang, S. Ryu, S. I. Seok, *Nat Mater* **2014**, 13, 897; e) W. S. Yang, J. H. Noh, N. J. Jeon, Y. C. Kim, S. Ryu, J. Seo, S. I. Seok, *Science* **2015**, 348, 1234; f) G. E. Eperon, T. Leijtens, K. A. Bush, R. Prasanna, T. Green, J. T.-W. Wang, D. P. McMeekin, G. Volonakis, R. L. Milot, R. May, A. Palmstrom, D. J. Slotcavage, R. A. Belisle, J. B. Patel, E. S. Parrott, R. J. Sutton, W. Ma, F. Moghadam, B. Conings, A. Babayigit, H.-G. Boyen, S. Bent, F. Giustino, L. M. Herz, M. B. Johnston, M. D. McGehee, H. J. Snaith, *Science* **2016**, 354, 861.

[2] a) H. Min, D. Y. Lee, J. Kim, G. Kim, K. S. Lee, J. Kim, M. J. Paik, Y. K. Kim, K. S. Kim, M. G. Kim, T. J. Shin, S. Il Seok, *Nature* **2021**, 598, 444; b) M. Kim, J. Jeong, H. Lu, T. K. Lee, F. T. Eickemeyer, Y. Liu, I. W. Choi, S. J. Choi, Y. Jo, H.-B. Kim, S.-I. Mo, Y.-K. Kim, H. Lee, N. G. An, S. Cho, W. R. Tress, S. M. Zakeeruddin, A. Hagfeldt, J. Y. Kim, M. Grätzel, D. S. Kim, *Science* **2022**, 375, 302.

[3] J. Cao, H. L. Loi, Y. Xu, X. Guo, N. Wang, C. K. Liu, T. Wang, H. Cheng, Y. Zhu, M. G. Li, W. Y. Wong, F. Yan, *Adv Mater* **2021**, 34, 2107729.

[4] A. Rajagopal, Z. Yang, S. B. Jo, I. L. Braly, P. W. Liang, H. W. Hillhouse, A. K. Jen, *Adv Mater* **2017**, 29.

[5] a) Z. H. Yu, Z. B. Yang, Z. Y. Ni, Y. C. Shao, B. Chen, Y. Z. Lin, H. T. Wei, Z. S. J. Yu, Z. Holman, J. S. Huang, *Nat Energy* **2020**, 5, 657; b) R. Lin, J. Xu, M. Wei, Y. Wang, Z. Qin, Z. Liu, J. Wu, K. Xiao, B. Chen, S. M. Park, G. Chen, H. R. Atapattu, K. R. Graham, J. Xu, J. Zhu, L. Li, C. Zhang, E. H. Sargent, H. Tan, *Nature* **2022**, DOI: 10.1038/s41586-021-04372-8; c) Z. Yu, X. Chen, S. P. Harvey, Z. Ni, B. Chen, S. Chen, C. Yao, X. Xun, S. Xu, G. Yang, Y. Yan, J. J. Berry, M. C. Beard, J. Huang, *Adv Mater* **2022**, DOI: 10.1002/adma.202110351; d) L. Li, Y. Wang, X. Wang, R. Lin, X. Luo, Z. Liu, K. Zhou, S. Xiong, Q. Bao, G. Chen, Y. Tian, Y. Deng, K. Xiao, J. Wu, M. I. Saidaminov, H. Lin, C.-Q. Ma, Z. Zhao, Y. Wu, L. Zhang, H. Tan, *Nat Energy* **2022**, DOI: 10.1038/s41560-022-01045-2.

[6] J. Tong, Q. Jiang, A. J. Ferguson, A. F. Palmstrom, X. Wang, J. Hao, S. P. Dunfield, A. E. Louks, S. P. Harvey, C. Li, H. Lu, R. M. France, S. A. Johnson, F. Zhang, M. Yang, J. F. Geisz, M. D. McGehee, M. C. Beard, Y. Yan, D. Kuciauskas, J. J. Berry, K. Zhu, *Nat Energy* **2022**, DOI: 10.1038/s41560-022-01046-1.

[7] Y.-C. Chin, M. Daboczi, C. Henderson, J. Luke, J.-S. Kim, *Acs Energy Lett* **2022**, 7, 560.

[8] a) G. Kapil, T. Bessho, Y. Sanehira, S. R. Sahamir, M. Chen, A. K. Baranwal, D. Liu, Y. Sono, D. Hirotani, D. Nomura, K. Nishimura, M. A. Kamarudin, Q. Shen, H. Segawa, S. Hayase, *Acs Energy Lett* **2022**, 7, 966; b) R. Prasanna, T. Leijtens, S. P. Dunfield, J. A. Raiford, E. J. Wolf, S. A. Swifter, J. Werner, G. E. Eperon, C. de Paula, A. F. Palmstrom, C. C. Boyd, M. F. A. M. van Hest, S. F. Bent, G. Teeter, J. J. Berry, M. D. McGehee, *Nat Energy* **2019**, 4, 939.

[9] a) Q. Han, Y. Wei, R. Lin, Z. Fang, K. Xiao, X. Luo, S. Gu, J. Zhu, L. Ding, H. Tan, *Science Bulletin* **2019**, 64, 1399; b) H. Gao, Q. Lu, K. Xiao, Q. Han, R. Lin, Z. Liu, H. Li, L. Li, X. Luo, Y. Gao, Y. Wang, J. Wen, Z. Zou, Y. Zhou, H. Tan, *Sol Rrl* **2021**, 5, 2100814.

[10] J. Sun, C. Shou, J. Sun, X. Wang, Z. Yang, Y. Chen, J. Wu, W. Yang, H. Long, Z. Ying, X. Yang, J. Sheng, B. Yan, J. Ye, *Sol Rrl* **2021**, 5, 2100663.

[11] D. D. Astridge, J. B. Hoffman, F. Zhang, S. Y. Park, K. Zhu, A. Sellinger, *ACS Applied Polymer Materials* **2021**, 3, 5578.

[12] J. Werner, T. Moot, T. A. Gossett, I. E. Gould, A. F. Palmstrom, E. J. Wolf, C. C. Boyd, M. F. A. M. van Hest, J. M. Luther, J. J. Berry, M. D. McGehee, *Acs Energy Lett* **2020**, 5, 1215.

[13] a) J. Tong, J. Gong, M. Hu, S. K. Yadavalli, Z. Dai, F. Zhang, C. Xiao, J. Hao, M. Yang, M. A. Anderson, E. L. Ratcliff, J. J. Berry, N. P. Padture, Y. Zhou, K. Zhu, *Matter* **2021**, 4, 1365; b) C. Li, Z. Song, C. Chen, C. Xiao, B. Subedi, S. P. Harvey, N. Shrestha, K. K. Subedi, L. Chen, D. Liu, Y. Li, Y.-W. Kim, C.-s. Jiang, M. J. Heben, D. Zhao, R. J. Ellingson, N. J. Podraza, M. Al-Jassim, Y. Yan, *Nat Energy* **2020**, 5, 768.

[14] a) J. Warby, F. Zu, S. Zeiske, E. Gutierrez‐Partida, L. Frohloff, S. Kahmann, K. Frohna, E. Mosconi, E. Radicchi, F. Lang, S. Shah, F. Peña‐Camargo, H. Hempel, T. Unold, N. Koch, A. Armin, F. De Angelis, S. D. Stranks, D. Neher, M. Stolterfoht,

Adv Energy Mater **2022**, DOI: 10.1002/aenm.2021035672103567; b) S. Chen, X. Xiao, H. Gu, J. Huang, *Sci Adv* **2021**, 7, eabe8130.

[15] T. H. Schloemer, T. S. Gehan, J. A. Christians, D. G. Mitchell, A. Dixon, Z. Li, K. Zhu, J. J. Berry, J. M. Luther, A. Sellinger, *Acs Energy Lett* **2019**, 4, 473.

[16] a) J. Peng, J. I. Khan, W. Liu, E. Ugur, T. Duong, Y. Wu, H. Shen, K. Wang, H. Dang, E. Aydin, X. Yang, Y. Wan, K. J. Weber, K. R. Catchpole, F. Laquai, S. Wolf, T. P. White, *Adv Energy Mater* **2018**, 8, 1801208; b) J. Peng, D. Walter, Y. Ren, M. Tebyetekerwa, Y. Wu, T. Duong, Q. Lin, J. Li, T. Lu, M. A. Mahmud, O. L. C. Lem, S. Zhao, W. Liu, Y. Liu, H. Shen, L. Li, F. Kremer, H. T. Nguyen, D.-Y. Choi, K. J. Weber, K. R. Catchpole, T. P. White, *Science* **2021**, 371, 390; c) J. Peng, F. Kremer, D. Walter, Y. Wu, Y. Ji, J. Xiang, W. Liu, T. Duong, H. Shen, T. Lu, F. Brink, D. Zhong, L. Li, O. Lee Cheong Lem, Y. Liu, K. J. Weber, T. P. White, K. R. Catchpole, *Nature* **2022**, 601, 573.

[17] a) Q. Wang, C. Bi, J. S. Huang, *Nano Energy* **2015**, 15, 275; b) Y. Zhao, T. Heumueller, J. Zhang, J. Luo, O. Kasian, S. Langner, C. Kupfer, B. Liu, Y. Zhong, J. Elia, A. Osvet, J. Wu, C. Liu, Z. Wan, C. Jia, N. Li, J. Hauch, C. J. Brabec, *Nat Energy* **2021**, 7, 144.

[18] E. Ochoa-Martinez, M. Ochoa, R. D. Ortuso, P. Ferdowsi, R. Carron, A. N. Tiwari, U. Steiner, M. Saliba, *Acs Energy Lett* **2021**, 6, 2626.

[19] J. Wang, J. Xu, Z. Li, X. Lin, C. Yu, H. Wu, H.-l. Wang, *ACS Applied Energy Materials* **2020**, 3, 6344.

[20] C. Li, Z. Song, D. Zhao, C. Xiao, B. Subedi, N. Shrestha, M. M. Junda, C. Wang, C. S. Jiang, M. Al‐Jassim, R. J. Ellingson, N. J. Podraza, K. Zhu, Y. Yan, *Adv Energy Mater* **2018**, 9, 1803135.

[21] a) Q. Wang, Y. C. Shao, Q. F. Dong, Z. G. Xiao, Y. B. Yuan, J. S. Huang, *Energ Environ Sci* **2014**, 7, 2359; b) Y. Shao, Z. Xiao, C. Bi, Y. Yuan, J. Huang, *Nat Commun* **2014**, 5, 5784.

[22] C. Zhu, X. Niu, Y. Fu, N. Li, C. Hu, Y. Chen, X. He, G. Na, P. Liu, H. Zai, Y. Ge, Y. Lu, X. Ke, Y. Bai, S. Yang, P. Chen, Y. Li, M. Sui, L. Zhang, H. Zhou, Q. Chen, *Nat Commun* **2019**, 10.

[23] L. Meng, C. Sun, R. Wang, W. Huang, Z. Zhao, P. Sun, T. Huang, J. Xue, J. W. Lee, C. Zhu, Y. Huang, Y. Li, Y. Yang, *J Am Chem Soc* **2018**, 140, 17255.

[24] a) Y. M. Yang, X. Chen, S. Liu, H. Zhu, W. Wang, C. Kuang, X. Liu, *The Journal of Physical Chemistry C* **2021**, 125, 12560; b) J. Pascual, M. Flatken, R. Felix, G. Li, S. H. Turren-Cruz, M. H. Aldamasy, C. Hartmann, M. Li, D. Di Girolamo, G. Nasti, E. Husam, R. G. Wilks, A. Dallmann, M. Bar, A. Hoell, A. Abate, *Angew Chem Int Ed Engl* **2021**, 60, 21583; c) Q. Chen, J. Luo, R. He, H. Lai, S. Ren, Y. Jiang, Z. Wan, W. Wang, X. Hao, Y. Wang, J. Zhang, I. Constantinou, C. Wang, L. Wu, F. Fu, D. Zhao, *Adv Energy Mater* **2021**, 11, 2101045.

[25] R. Chen, Y. Wang, S. Nie, H. Shen, Y. Hui, J. Peng, B. Wu, J. Yin, J. Li, N. Zheng, *J Am Chem Soc* **2021**, 143, 10624.

[26] a) S. Chen, X. Dai, S. Xu, H. Jiao, L. Zhao, J. Huang, *Science* **2021**, 373, 902; b) Y.-H. Lin, N. Sakai, P. Da, J. Wu, H. C. Sansom, A. J. Ramadan, S. Mahesh, J. Liu, R. D. J. Oliver, J. Lim, L. Aspitarte, K. Sharma, P. K. Madhu, A. B. Morales‐Vilches, P. K. Nayak, S. Bai, F. Gao, C. R. M. Grovenor, M. B. Johnston, J. G. Labram, J. R. Durrant, J. M. Ball, B. Wenger, B. Stannowski, H. J. Snaith, *Science* **2020**, 369, 96.

[27] L. Gao, T. H. Schloemer, F. Zhang, X. Chen, C. Xiao, K. Zhu, A. Sellinger, *ACS Applied Energy Materials* **2020**, 3, 4492.

A custom prepared HTM polymer termed CzAn is used to replace the widely used PEDOT:PSS for Sn-Pb perovskite solar cells. PSCs using CzAn as HTM achieve a remarkable efficiency of 22.6%, higher than the PEDOT:PSS counterpart of 21.24%. Furthermore, CzAn based PSCs show lower trap density and facilitated carrier transport, thus enhancing the device current density and stability.

*Jiantao Wang, Zhenhua Yu, Daniel D. Astridge, Zhenyi Ni, Liang Zhao, Bo Chen, Mengru Wang, Ying Zhou, Guang Yang, Xuezeng Dai, Alan Sellinger and Jinsong Huang**

A Carbazole-Based Hole Transport Polymer for Methylammonium-Free Tin-Lead Perovskite Solar Cells with Enhanced Efficiency and Stability

ToC figure

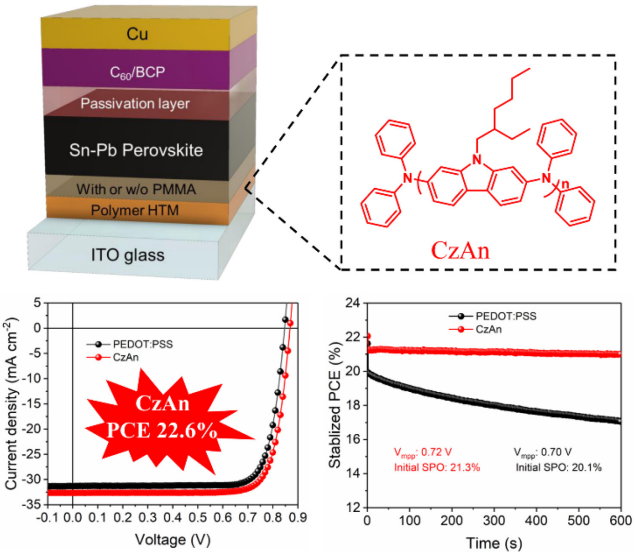

Supporting Information

A Carbazole-Based Hole Transport Polymer for Methylammonium-Free Tin-Lead Perovskite Solar Cells with Enhanced Efficiency and Stability

*Jiantao Wang, Zhenhua Yu, Daniel D. Astridge, Zhenyi Ni, Liang Zhao, Bo Chen, Mengru Wang, Ying Zhou, Guang Yang, Xuezeng Dai, Alan Sellinger and Jinsong Huang**

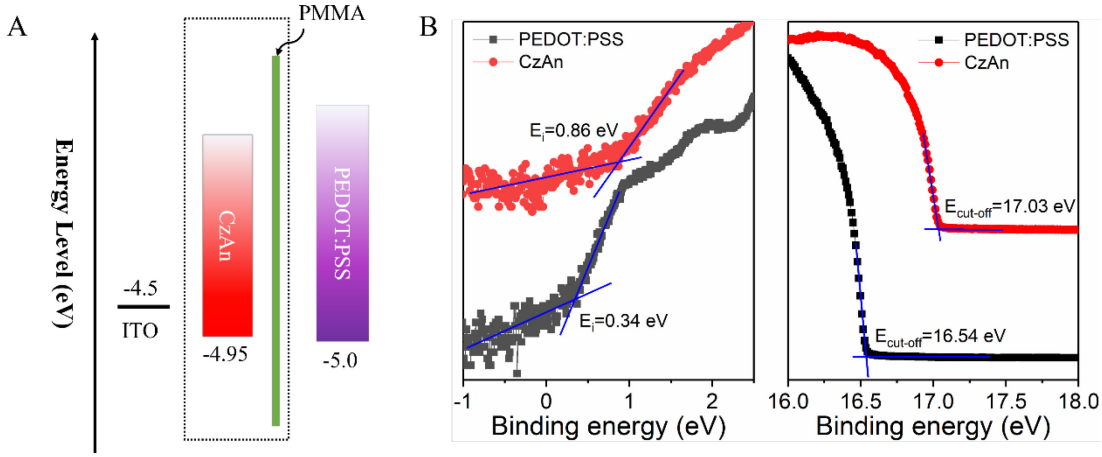

Figure S1. (A) Band energy alignment of ITO/HTMs. The bandgap of the intrinsic HTM CzAn is 2.94 eV. (B) UPS of modified CzAn and PEDOT:PSS deposited on ITO substrates. After modification, the HOMO of ITO/doped CzAn/PMMA is -5.03 eV, slightly shallower than ITO/PEDOT:PSS of -5.0 eV. The HOMOs were calculated according to the formula HOMO=$E_{cut\text{-}off}$-21.2-E_i (eV), where $E_{cut\text{-}off}$ and E_i are cut-off and onset energy boundaries in UPS results.

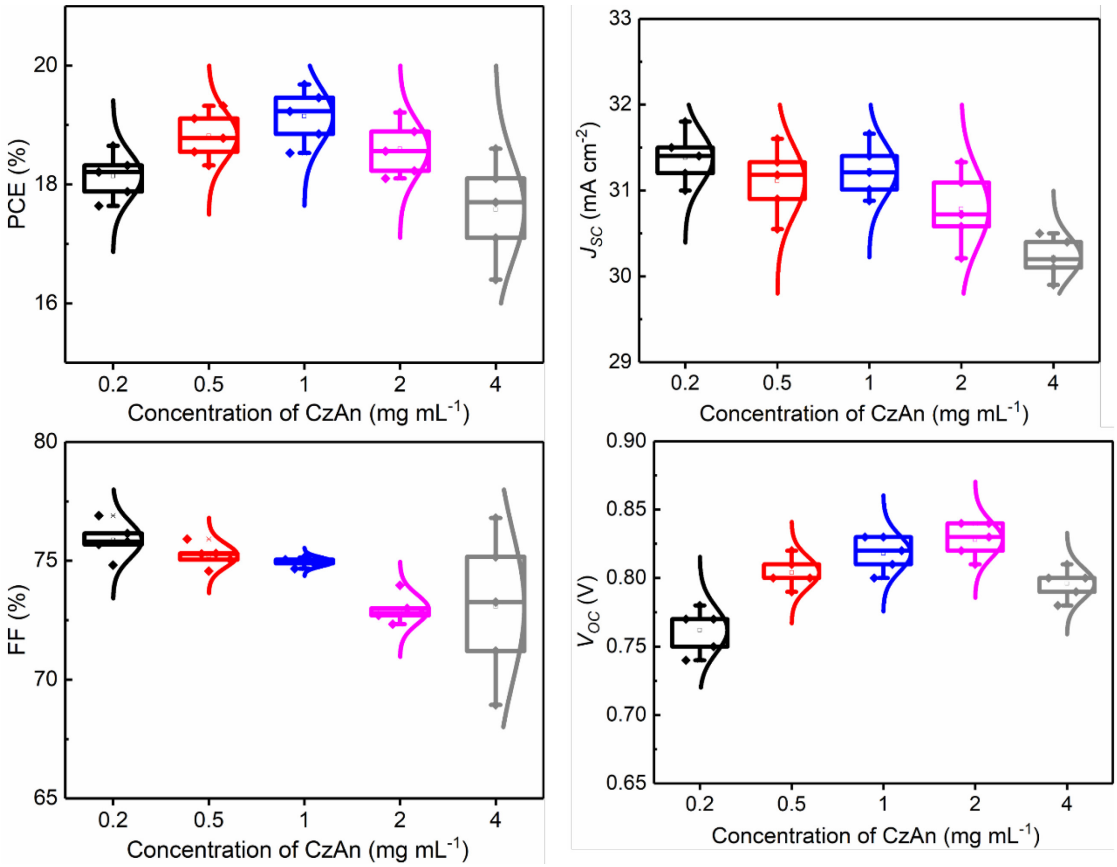

Figure S2. Photovoltaic (PV) parameters for Sn-Pb PSCs based on CzAn with varied concentration ranging from 0.2 to 4 mg mL^{-1}. For each concentration of CzAn, 5 devices were fabricated for the statistics of their PV parameters. The PV parameters for all the perovskites were determined by the *J-V* measurements under reverse scanning at 0.05 V s^{-1}.

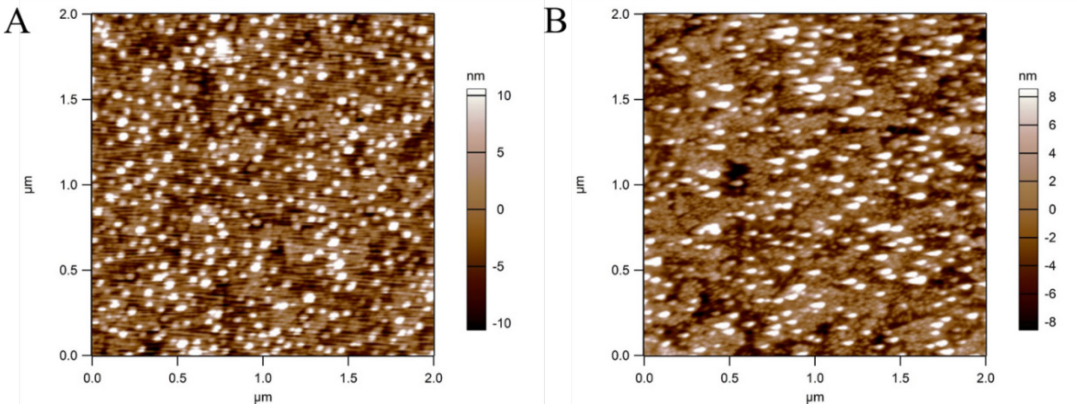

Figure S3. Morphologies of the CzAn polymer HTM (A) without and (B) with PMMA, respectively, measured by atomic force microscopy (AFM). PMMA was processed from a solution concentration of 0.2 mg mL^{-1} in acetonitrile.

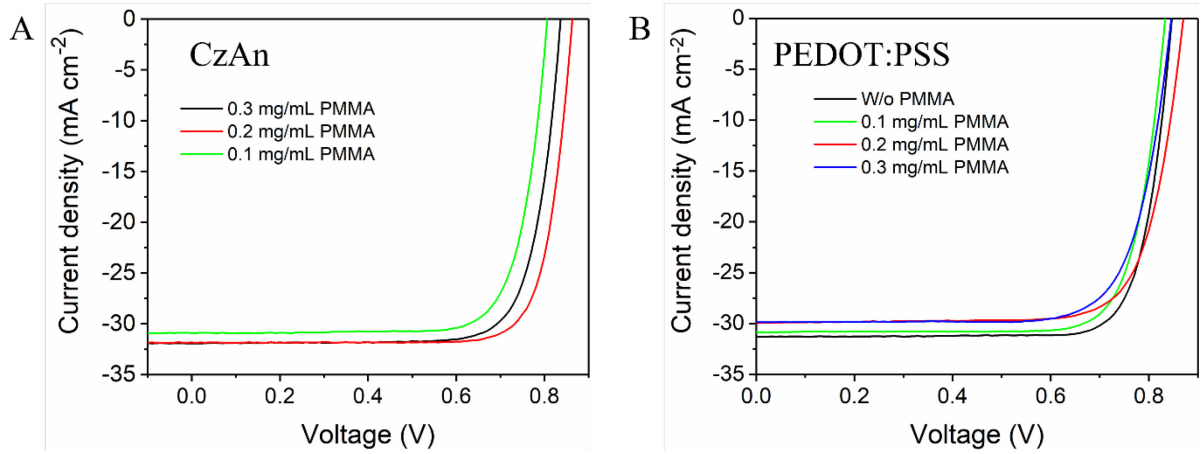

Figure S4. *J-V* curves of (A) CzAn and (B) PEDOT:PSS based devices using a PMMA top layer derived from different concentrations 0.1, 0.2 and 0.3 mg mL^{-1}.

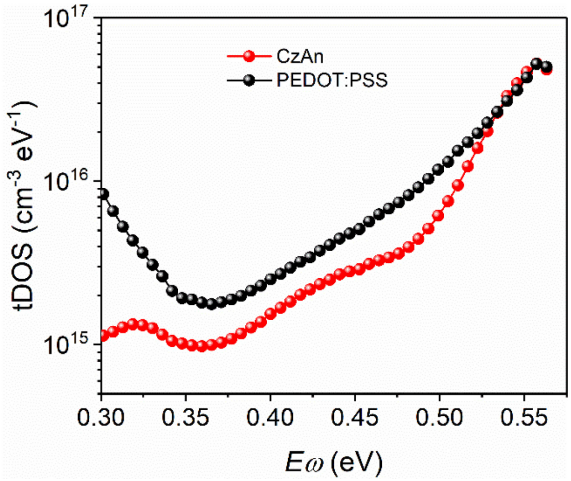

Figure S5. Trap density of states (tDOS) of photovoltaic devices based on modified CzAn and PEDOT:PSS.

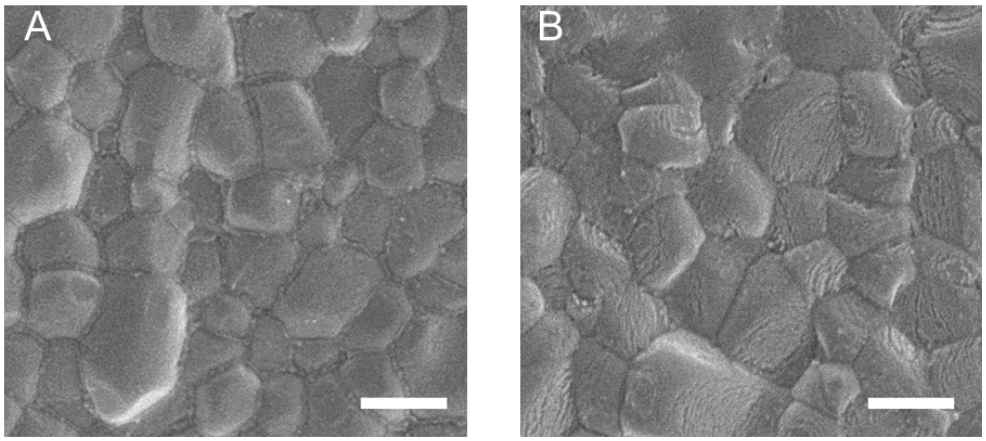

Figure S6. SEM surface morphology of perovskite films deposited on (A) CzAn/PMMA and (B) PEDOT:PSS. Scale bar: 500 nm.

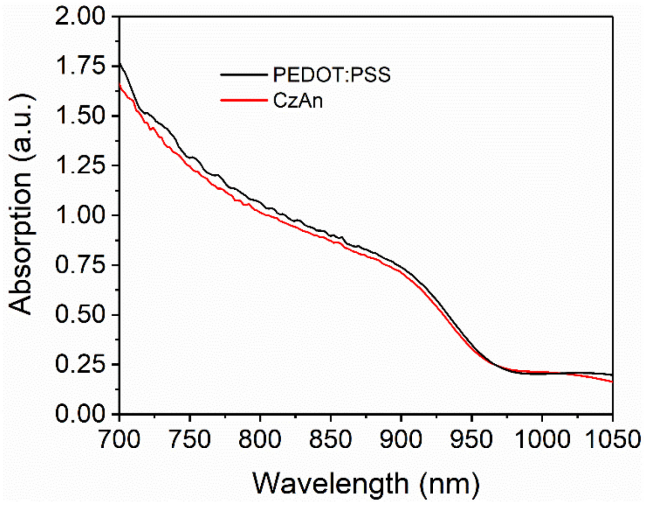

Figure S7. UV-Vis-NIR absorption of perovskite films deposited on CzAn/PMMA and PEDOT:PSS.

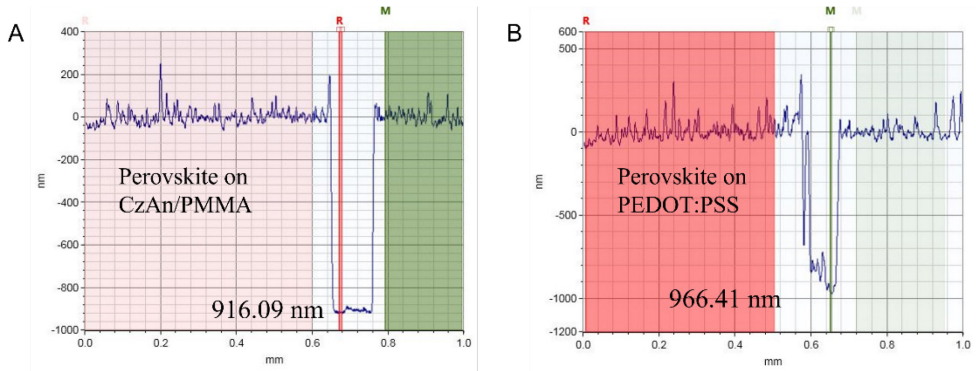

Figure S8. Thickness profiles of perovskite films deposited on (A) CzAn/PMMA and (B) PEDOT:PSS detected by a Stylus Profiler.

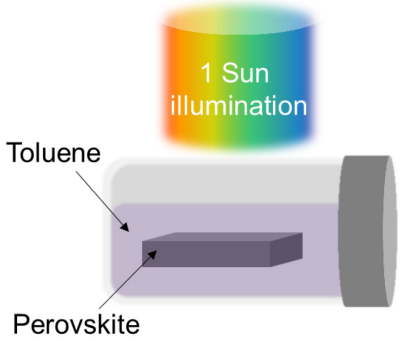

Figure S9. Illustration of experimental set up of film stability measurements.

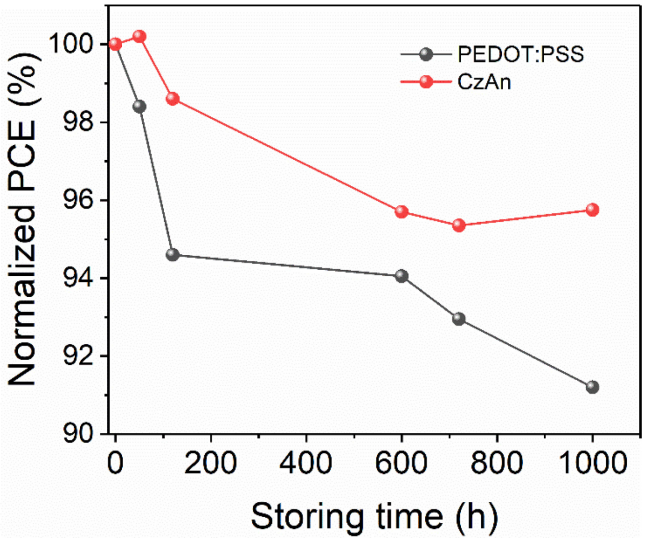

Figure S10. Normalized PCE of PSCs stored in ambient condition at different time.

Table S1. Photovoltaic parameters of PSCs based on PEDOT: PSS and CzAn before and after 1000 h storing time.

Devices	Measuring time	V_{oc} [V]	J_{sc} [mA cm^{-2}]	FF [%]	PCE [%]
PEDOT:PSS	0 h	0.84	30.65	81.64	21.02
	1000 h	0.84	28.57	79.92	19.18
CzAn	0 h	0.87	32.64	79.62	22.61
	1000 h	0.86	31.73	79.34	21.65